

INITIAL STEADY/UNSTEADY CFD ANALYSIS OF VORTEX FLOW OVER THE VFE-2 DELTA WING

Simone Crippa , Arthur Rizzi

*Department of Aeronautical and Vehicle Engineering, Royal Institute of Technology (KTH)

Keywords: VFE-2, CFD, 65° delta wing

Abstract

This study is aimed at assessing the application of the latest unstationary CFD method, Detached-Eddy Simulation (DES), to simulate the flow-field around blunt leading edge delta wings. For this purpose, the Second International Vortex Flow Experiment (VFE-2) 65° sweep delta wing model was used to perform numerical investigations at a Reynolds number of 6 million, Mach number of 0.4 and angles of attack of 18.5° and 23°. As the nature of this study is mainly exploratory, various numerical grids have been used. The results confirm the maturity of Reynolds averaged Navier-Stokes (RANS) methods but also the problems of DES to predict free separation and the grid sensitivity of this model.

1 Introduction

To study the behavior of high-performance aircrafts featuring delta wing planforms, in the past the selected simplified geometry was the sharp leading edge, slender delta wing. This geometry does not resemble one main feature of real-application delta wing planforms, the finite radius of the leading edge. The sudden shear layer separation present in sharp leading edge delta wings, generates distinct separated vortex flow starting from the delta wing apex. As this distinct separation onset is not given in case of a blunt leading edge delta wing, computational fluid dynamic (CFD) methods necessitate to resolve the boundary layer development prior to separation onset to accurately predict the overall flow-field characteristics. At high angles of attack, this can

be coupled to unstationary phenomena such as vortex breakdown.

The deployment of initial hybrid RANS/LES methods, of which probably the most widely used is DES by Spalart et al. [12], might be ill-posed for flow separation from blunt leading edge delta wings. This is due to Reynolds number dependence of initial shear layer separation and vortex location/strength for blunt leading edge delta wings.[2, 11] Here the underlying RANS model of DES (Spalart-Allmaras) may not be appropriate to predict curvature-induced, free separation. Whereas on sharp leading edge delta wings, the separation line is fixed at the leading edge. The comparison of DES with newly developed turbulence models for RANS closure is thus needed to evaluate advantages and deficiencies of each approach.

This need has been recognized by the NATO Research and Technology Organization (RTO) panel, which in September 2002 approved the formation of a task group with the notation AVT-113. One of the two facets of this task group is denominated VFE-2 following the (first) International Vortex Flow Experiment, which was focussed on Euler code validation [4]. Objectives and initial results of the VFE-2 facet are already available [6]. The initial wind tunnel campaign on which this evaluation is based on, has been performed by Chu and Luckring [1], NASA Langley Research Center (LaRC) in the National Transonic Facility (NTF).

2 Model Description

The geometry proposed by Hummel and Re-deker [7] for the VFE-2 project is that of a delta wing with a 65° leading edge sweep angle (Λ). This configuration is the same as in the NTF wind tunnel campaign [1] and a sketch of the delta wing is shown in figure 1. A remarkable feature of the wind tunnel model is the possibility to interchange the leading edge sections, representing four leading edge radii (r_{LE}), which are attached to the flat-plate central section.

The half-body, numerical geometric definition of the model is available through a Virtual Laboratory [9] set up and maintained by NASA LaRC. The origin of the right-handed, Cartesian coordinate system is at the apex of the delta wing with the x-coordinate pointing downstream (towards the sting), the z-coordinate being perpendicular to the flat plate section and the y-coordinate pointing in span-wise direction. The numerical geometry features a root chord (c_r) of $1m$ resulting in a mean aerodynamic chord (\bar{c}) of $2/3m \approx 0.667m$.

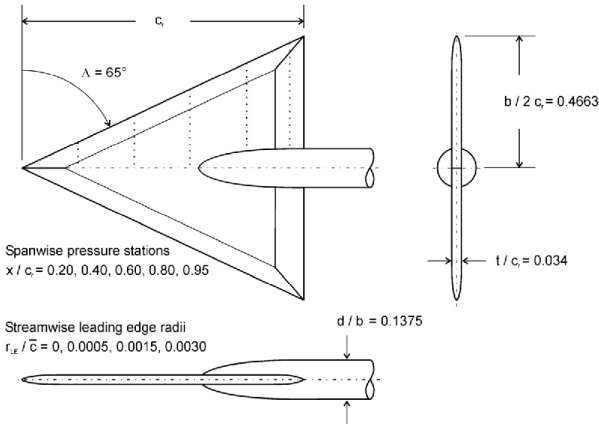


Fig. 1 NASA's wind tunnel model, geometry description. [8]

For the VFE-2 project, the sharp ($r_{LE}/\bar{c} = 0$) (sLE) and medium radius ($r_{LE}/\bar{c} = 0.0015$) leading edge (mLE) geometries were selected for numerical and further wind tunnel evaluations.

2.1 Test Cases

The VFE-2 task group selected a matrix of computational cases based on realistic application

problems and CFD development and evaluation needs. Each of the two main geometry configurations (sLE and mLE) is mainly used to study distinct effects. The conditions for the blunt leading edge geometry were chosen for studying primarily the transition from attached flow to semi-separated vortical flow up to fully-separated dead-water flow. The sharp leading edge free-stream conditions were chosen for studying unsteady phenomena such as vortex breakdown and transonic vortex-shock interactions.

For this study the subsonic Mach number (M) of 0.4, $Re_{\bar{c}}=6 \cdot 10^6$ cases were selected, where the reference length for the Reynolds number ($Re_{\bar{c}}$) is the mean aerodynamic chord. The main cases for this study were initially the $\alpha=23.3^\circ$ cases (case 13 and 17), to explore the initial vortex breakdown conditions. Then the computational matrix was expanded to include also a lower angle of attack (at $Re_{\bar{c}}=6 \cdot 10^6$ and $M=0.4$) of $\alpha=18.5^\circ$, due to the increased separation onset dependence on leading edge geometry.

To ease future comparison, the results shown here retain the VFE-2 test matrix nomenclature, of which the relevant sections for this study are listed in table 1.

Table 1 Test cases ($M=0.4$, $Re_{\bar{c}}=6 \cdot 10^6$)

Case	Geometry	AOA
01	sLE	18.5°
13	sLE	23.0°
05	mLE	18.5°
17	mLE	23.0°

The free-stream conditions from the experimental campaign differ slightly from the VFE-2 computational matrix. The cases used for this comparison are summarized in table 2.

Table 2 Experimental cases selected for comparison from Chu and Luckring [1] ($Re_{\bar{c}} = 6 \cdot 10^6$)

Run No.	Point No.	Geom.	AOA	M
84	1834	sLE	18.4°	0.400
84	1838	sLE	22.5°	0.401
3	54	mLE	18.4°	0.400
3	56	mLE	22.4°	0.400

2.2 Computational Method

The flow solver EDGE [3] was used throughout this study. EDGE is an unstructured, edge-based, finite volume CFD code developed and maintained by the Swedish Defence Research Agency (FOI). KTH is one among several academic contributors to the development of the code. All computations run during this study were performed with the latest development version of EDGE, 3.3.2-r506, fully parallelized using the Scali MPI libraries.

For the steady-state calculations, the turbulence model used for the closure of the RANS equations is the two-equation $k - \omega$ model by Hellsten [5] coupled to the explicit algebraic Reynolds stress model (EARSM) by Wallin and Johansson [17]. For selected cases, the Spalart-Allmaras (SA) model [14] has also been used.

All calculations have been performed with the assumption of fully turbulent flow, with a free-stream turbulence intensity of 0.1%.

Time integration to steady state of the discretized RANS equations was achieved with an explicit, three-stage Runge-Kutta scheme. For the spatial discretization, a second order accurate, central scheme with 4th order artificial dissipation set to 0.03 was used for all cases. To speed up convergence, implicit residual smoothing and four level FAS agglomeration multigrid were used.

The original DES formulation by Spalart et al. [12] is implemented in EDGE, whereby time integration is achieved through “dual time stepping”, an implicit time marching technique with explicit sub-iterations.

Solution based adaptive grid refinement [16] is also available in EDGE and has been used to refine the initial computational grid of the steady, blunt leading edge cases. This option was not available for the sharp leading edge cases, as the imported computational grid was not compatible to the adaptation program. The adaptation algorithm features three different vortex-capturing sensors [10] based on total pressure ratio, entropy loss and an eigenvalue analysis of the velocity gradient tensor. Using a flow solution mapped

on the corresponding numerical grid and a user-defined value for the selected sensor, the adaptation algorithm selects the cell edges to be subdivided.

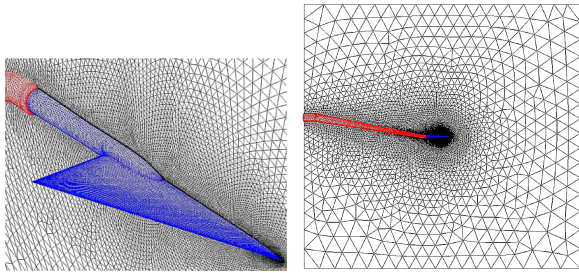
2.3 Numerical Grid and Boundary Conditions

Two similar numerical grid topologies have been employed within this study. Both grids feature a half-span representation of the delta wing model with a symmetric boundary condition applied on the symmetry plane. Furthermore, the boundary for the solid walls is of adiabatic, no-slip type and on the far-field boundary a weak formulation characteristic condition was set.

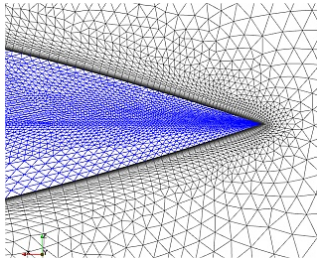
The computational grid for the sharp leading edge geometry has been made available to the partners of the VFE-2 group by the U. S. Air Force Academy (USAF). A common unstructured grid is not available for the blunt leading edge geometry, thus it was generated using either the commercially available ICEM CFD meshing package or the FOI-internal advancing-front grid generator TRITET [15]. The latter is the tool of choice for generating hybrid grids for EDGE, as it is transparently interfaced to the adaptation program available within the EDGE distribution.

2.4 Sharp Leading Edge

The common sharp leading edge grid features approx. 7.89 million tetrahedral and 0.8 million prismatic cells. The surface of the half-span delta wing and the sting fitting is discretized with 67,489 triangular elements, resulting in 19 full prismatic layers to resolve the boundary layer. The surface mesh of the delta wing, the sting fitting and the sting-closure as well as the symmetry mesh are visible in figure 2(a). Note that the sting-closure does not feature a prismatic layer discretization and is extended to the far-field outflow boundary, see figure 2(b). The extents of the far-field boundary-box are located at approx. 10 root chord lengths from the delta wing surface. In y-direction (wingspan direction) the far-field boundary is located at approx. 5 root chord lengths.



(a) Delta wing surface grid (b) Sting surface grid and near-field symmetry plane up to far-field boundary, isometric view



(c) Surface grid of delta wing apex and symmetry plane, side view (up to $x/c_r \approx 0.05$).

Fig. 2 Common computational grid for the sharp leading edge cases.

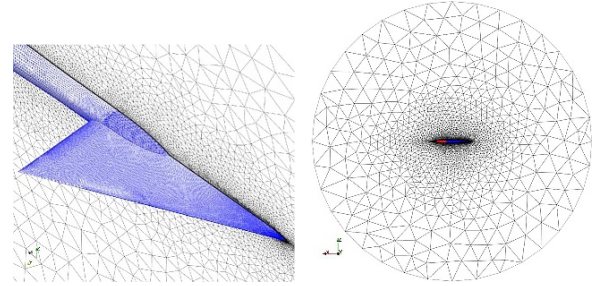
2.5 Medium Leading Edge

In contrast to the VFE-2 common sharp leading edge grid, the sting closure for the blunt leading edge cases has been chosen not to extend downstream to the far-field boundary. The sting is represented exactly as in the wind tunnel model up to the position $x/c_r = 1.758$, as recommended by Chu and Luckring [1]. After this position, the sting is closed out using an elliptical revolution surface, which is continuous through the curvature at the cut-off station. The total length (in x-direction) of the closure surface is five times the diameter of the sting at the cut-off position.

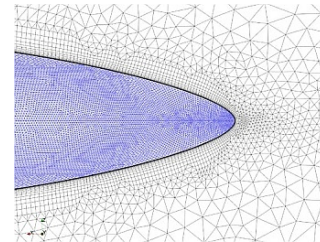
The far-field boundary is located at approx. 11 root chord lengths from any wall, in all directions, resulting in a half-sphere far-field boundary with a radius of $12.5m$.

RANS grids. The basic meshing strategy for the steady-state medium leading edge cases was to first generate a volume grid with a coarse tetrahedral discretization to yield first results,

with which solution based adaptation was subsequently possible. Based on initial results, the first cell height needed to achieve y^+ values smaller than 1, was identified to be $1 \cdot 10^{-6}m$. The 32 prismatic element layers were used to resolve the viscous layer up to a normal distance to the wall of $0.015m$, resulting in an exponential expansion ratio normal to the wall of 1.30. The initial surface grid is visible in figure 3.



(a) Delta wing surface grid (b) Symmetry grid up to and near-field symmetry far-field boundary, isometric view.



(c) Surface grid of delta wing apex and symmetry plane, side view (up to $x/c_r \approx 0.15$).

Fig. 3 Computational grid for case 17, EARS (initial) and DES.

As visible in figure 3(c), the meshing approach used in TRITET automatically generates varying numbers of prismatic elements normal to the wall, thus ensuring a smooth volumetric transition between cell elements at the prismatic/tetrahedral interface.

After evaluating all available adaptation sensors, the sensor based on the total pressure ratio ($p_0/p_{0\infty}$) was selected to refine the initial numerical grid. The threshold value for $p_0/p_{0\infty}$ used for selecting the cell edges to be split was set to 0.95. Surface projection for new nodes on the surfaces was disabled and for limiting the amount of selected edges, the minimal edge size to be adapted

was set to $0.001m$.

The adaptation was mostly constrained to the tetrahedral elements thanks to the definition of adaptation bounding boxes. Grid elements outside of these boxes would not be considered for adaptation. The coordinates of the adaptation boxes are summarized in table 3.

Table 3 Coordinates of adaptation boxes for cases 05 and 17 (EARSM)

$x_{min} - x_{max}$ [m]	$y_{min} - y_{max}$ [m]	$z_{min} - z_{max}$ [m]
-11.5 – 0.63	0.0 – 11.5	0.038 – 11.5
-11.5 – 0.63	0.0 – 11.5	-11.5 – -0.038
0.63 – 1.017	0.08 – 11.5	0.038 – 11.5
0.63 – 1.017	0.08 – 11.5	-11.5 – -0.038
0.63 – 1.017	0.0 – 0.08	0.07 – 11.5
0.63 – 1.017	0.0 – 0.08	-11.5 – -0.07
1.017 – 11.5	0.11 – 11.5	-11.5 – 11.5
1.017 – 11.5	0.0 – 0.11	0.11 – 11.5
1.017 – 11.5	0.0 – 0.11	-11.5 – -0.11
2.6 – 11.5	0.0 – 0.11	-0.11 – 0.11

The resulting additional tetrahedral cells for the adaptation of case 17, as well as the outlines of the adaptation boxes near the solid walls are visible in figure 4.

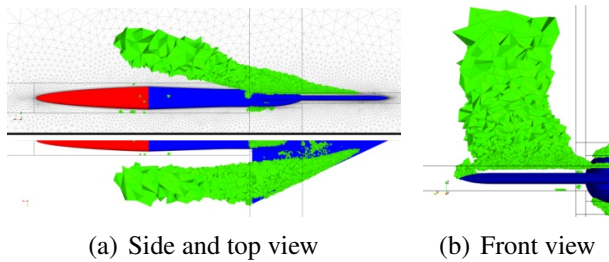
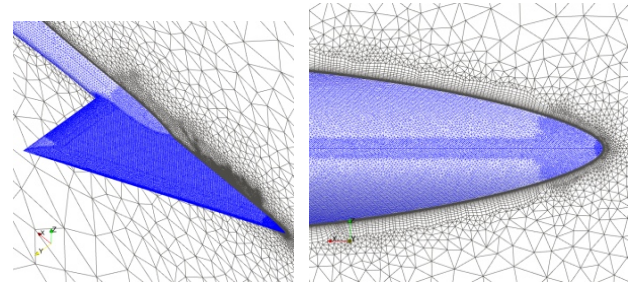


Fig. 4 Additional tetrahedral elements after adaptation; case 17.

DES grids. For the DES runs, a priori adaptation based on EARSM results was not considered in this study as h-adaptation leads to a high number of anisotropic tetrahedral cells. This was recognized to be undesirable for DES [13], thus for case 05 a globally finer grid was generated with ICFM CFD. The use of density regions above

the suction side of the delta wing ensures an homogeneous tetrahedral distribution. See figure 5. The first cell height was set to $2.7 \cdot 10^{-7}m$ at the



(a) Isometric view of delta wing surface grid and near-apex and symmetry plane (b) Surface grid of delta wing surface grid and near-apex and symmetry plane, side field symmetry plane view (up to $x/c_r \approx 0.22$).

Fig. 5 Computational grid for case 05, DES.

leading edge and $5 \cdot 10^{-6}m$ on the flat-plate inner delta wing portion as well as on the sting. 32 prismatic layers discretize the boundary layer region with a total extent normal to the walls on approx. $0.02m$.

For the grid of case 17 on the other hand, the same initial computational grid as for the EARSM case was selected. This was mainly due to computational and time constraints.

The sizes for the grids employed in this study are summarized in table 4.

3 Results and Discussion

For the comparison between RANS, DES and experimental data, the unstationary data from the DES cases was averaged over at least one full period of the monitored force coefficients.

3.1 Time-Step

An initial evaluation of the required outer time-step for the DES cases was performed for case 13. Two DES calculations were performed with an initial smaller model ($c_r = 0.3048m$) with both a small time-step ($\Delta t = 5 \cdot 10^{-6}s$) and a larger time-step ($\Delta t = 5 \cdot 10^{-5}s$) to assess the tradeoff between accuracy and computational effort. The non-dimensional time-steps ($\Delta t^* = [U_\infty \cdot \Delta t]/c_r$) are $2.252 \cdot 10^{-3}$ and $2.252 \cdot 10^{-2}$, respectively for the small and large time-step.

Table 4 Computational grid size for the cases analyzed in this study (pyramidal elements are included in the total volume cells counts)

Grid	“solid wall” tri. elem.	Prismatic vol. cells	Tetrahedral vol. cells	Total vol. cells (nodes)
Case 01/13, RANS/DES	72,122	820,273	7,025,184	7,886,068 (1,643,487)
Case 05/17, RANS; Initial	171,596	5,246,330	2,364,969	7,657,846 (3,093,054)
Case 05, RANS; adapted	182,454	5,593,765	3,160,627	8,800,958 (3,405,554)
Case 17, RANS; adapted	178,244	5,459,039	2,848,078	8,353,689 (3,283,478)
Case 05, DES	235,015	7,520,480	5,234,624	12,755,104 (4,721,858)
Case 17, DES	171,596	5,246,330	2,364,969	7,657,846 (3,093,054)

Comparing e.g., the vortex burst location between the three calculations, revealed an expected increase of accuracy from the less computational intensive EARSM (approx. 138 CPU-hours) to the larger time-step DES run (approx. 357 CPU-hours) and to the small time-step DES run (approx. 3360 CPU-hours).

These initial runs confirmed the selection of the smaller time-step for further DES computations. Due to the larger root chord of the numerical model employed in this study, the resulting outer (dimensional) time-step was set to $1.62 \cdot 10^{-5} s$.

3.2 Sharp Leading Edge

3.2.1 Case 01

The surface pressure coefficient for this case is shown in figure 6. Here the match of primary vortex strength is shown to correlate well for $x/c_r = 0.4$ and 0.6 for both EARSM and DES runs. At $x/c_r = 0.2$, DES shows a poorly resolved primary vortex, but at $x/c_r = 0.8$, DES still predicts the strength of the primary vortex accurately enough and EARSM already shows a weakening suction peak. At $x/c_r = 0.95$ both EARSM and DES do not show evidence of vortex breakdown. For this condition, further analysis of the DES results confirms vortex breakdown position to be at approx. $x/c_r = 0.97$. The convergence history for the DES run of case 01 is visible in figure 7.

3.2.2 Case 13

For case 13, the comparison between RANS, time-averaged DES and experimental surface pressure coefficient data at five different sections is presented in figure 8. For this case, the DES solution matches well the EARSM solution in terms of primary vortex strength and location, but the EARSM solution resolves better secondary separation. Both CFD solutions underestimate the strength of the primary vortex downstream of $x/c_r = 0.6$.

3.3 Medium Leading Edge

For the medium leading edge cases, previous investigations [8, 2] on this geometry have shown that an inner vortical system is already present when the leading edge (outer) primary vortex is formed. This (inner) second vortical structure was described first by Hummel [6]. The notation used in the following conforms to previous definitions by denoting the inner vortical structure, inner (primary) vortex, as the sense of rotation is equal to that of the outer primary vortex.

3.3.1 Case 05

For case 05 the difference between steady, unsteady and experimental data is more pronounced than for case 17. The main discrepancy is visible at $x/c_r = 0.2$, see figure 9(a). Here the experimental data shows a suction peak at approx. $\eta = 0.5$, revealing the presence of the inner primary vortex and a stronger suction peak between approx. $\eta = 0.85$ and $\eta = 0.9$ corresponding to the outer primary vortex. In contrast, the

Initial Steady/Unsteady CFD Analysis of Vortex Flow over the VFE-2 Delta Wing

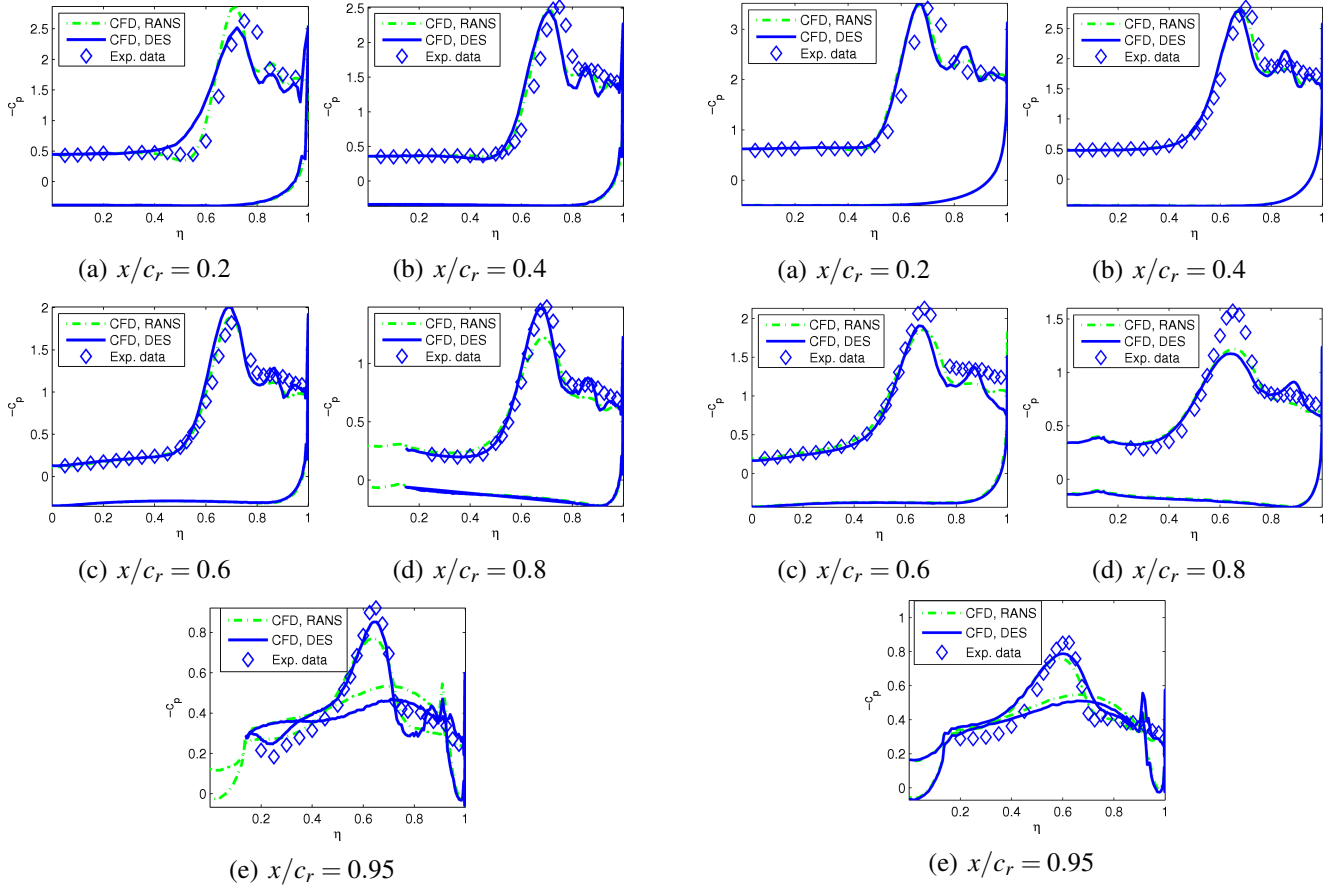


Fig. 6 Case 01; pressure coefficient plots at different chord-wise locations for the sLE geometry; comparison between RANS (EARSM), DES and experimental data (suction side only).

Fig. 8 Case 13; pressure coefficient plots at different chord-wise locations for the sLE geometry; comparison between RANS (EARSM), DES and experimental data (suction side only).

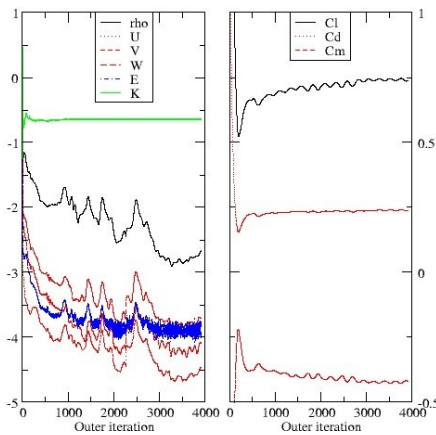


Fig. 7 Residuals and force coefficients convergence; case 01, DES.

EARSM + $k - \omega$ RANS solution shows a weaker outer primary vortex, but no visible evidence of the inner primary vortex. For this case, the dif-

ference between SA and EARSM + $k - \omega$ model were most pronounced. In the inner region, SA and DES match up to approx. $\eta = 0.75$, where SA starts predicting a weak primary vortex. On the other hand, DES predicts here fully attached flow over the entire semi-span.

At $x/c_r = 0.4$ DES predicts separated vortical flow leading to a stronger outer primary vortex suction peak and an inner suction peak corresponding to the inner primary vortex.

Further downstream, at $x/c_r = 0.6$, both CFD solutions match well the experimental data.

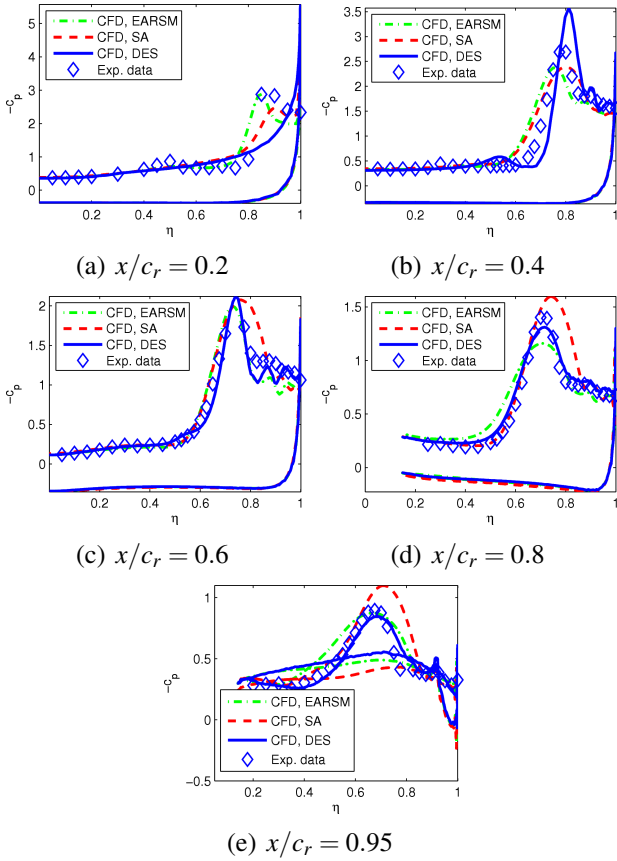


Fig. 9 Case 05; pressure coefficient plots at different chord-wise locations for the mLE geometry; comparison between RANS (SA and EARSM), DES and experimental data (suction side only).

3.3.2 Case 17

At $x/c_r = 0.2$ both CFD solutions predict leading edge separation, see figure 10(a). The pressure coefficient plot at $x/c_r = 0.2$ for this case is comparable with position $x/c_r = 0.4$ of case 05, where both CFD solutions predict leading edge separation. As in the previous case, DES predicts a stronger (and further outboard) inner primary vortex compared with experimental data, whereas EARSM predicts better the inner primary vortex location, but under-predicts the outer primary vortex suction peak.

After $x/c_r = 0.6$, no remarkable increase in accuracy is visible between DES and EARSM. This is probably due to the coarse computational grid above the rearward part of the delta wing, which in case of DES is not enough to resolve

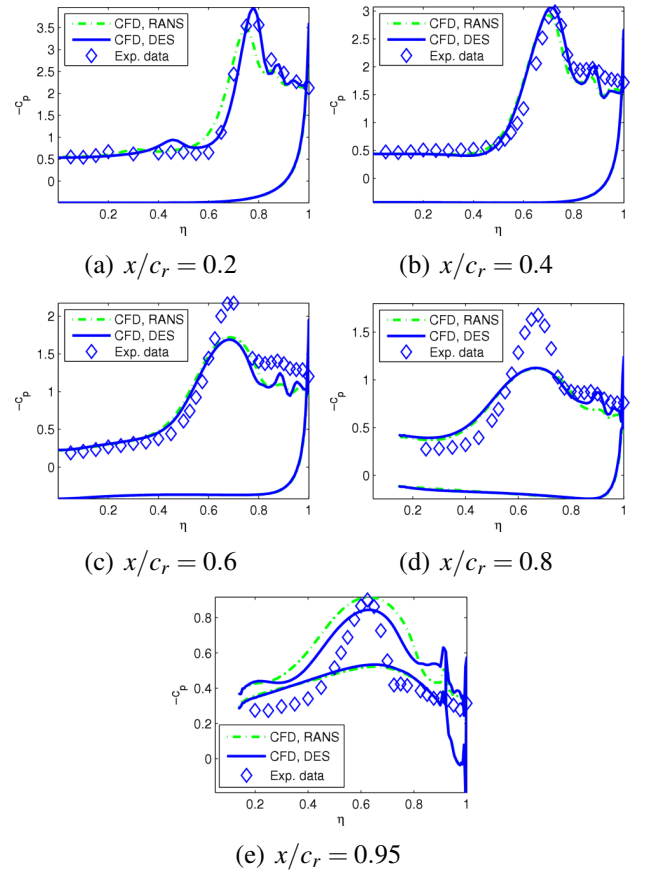


Fig. 10 Case 17; pressure coefficient plots at different chord-wise locations for the mLE geometry; comparison between RANS (EARSM), DES and experimental data (suction side only).

the relevant turbulent structures. At $x/c_r = 0.8$ and 0.95 , the pressure signature on the surface is flattened and broadened because of the presence of vortex breakdown. This phenomenon is likewise predicted by EARSM and DES, although at $x/c_r = 0.8$ the experimental values do not display evidence of vortex breakdown.

Convergence history for the EARSM run of case 17 is visible in figure 11.

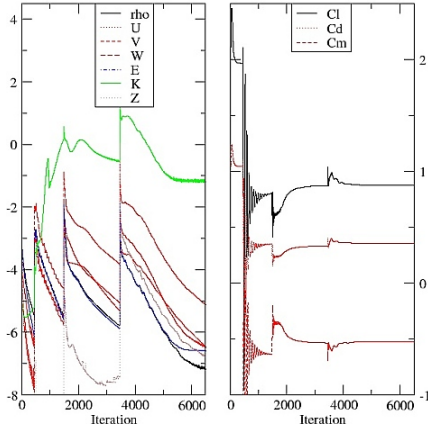


Fig. 11 Residuals and force coefficients convergence; case 17, EARSM.

3.4 Cross Comparison

Comparing at the same conditions the sharp and blunt leading edge cases, reveals consistent behavior of EARSM and DES. The apex region ($x/c_r = 0.2$) at the lower AOA of 18.5° (case 01 and 05) is resolved better by EARSM rather than DES, see figures 6(a) and 9(a). This trend is reversed in the rear region ($x/c_r = 0.8$), see figures 6(d) and 9(d).

The discrepancies between numerical and experimental results are alleviated by increasing the AOA to 23° (case 13 and 17). Due to the forward shift of vortex separation onset in case of the blunt leading edge case, the difference between EARSM and DES at the apex are less pronounced; see figures 8(a) and 10(a).

4 Conclusions

The results presented in this paper are mainly going to be used for future decision-making processes. Both for the sLE geometry as well as for the mLE geometry, this evaluation highlights the strengths and weaknesses of DES and RANS.

DES is better suited for the sLE geometry as the separation line of the primary vortex is fixed at the leading edge. This is in line with the original concept of DES. One reason for the similarly bad performance of DES compared to EARSM for case 13, might be a poorly resolved LES region in the aft vortex core path. The discrepancy from the experimental data is even more of

a concern since the VFE-2 common mesh has been used in this case. To use a computational grid generated for RANS to perform DES calculations was recognized to be sub-optimal. This approach is on the other hand expected, when either switching to DES as an incremental step after RANS, or when having to compute with common computational grids as in this case. Here, consistent isotropic h-adaptation would be a major future contribution.

For this case, as well as for all other investigated cases, the DES solutions consistently over-predict the strength of the secondary vortex and the suction due to the initial shear layer roll-up. Based on these results no substantial benefit can be obtained by the use of DES in regards of mean surface pressure coefficient. But the position and topology of vortex breakdown are resolved accurately with DES, giving also information about e.g., the rotation frequency of the spiral-type vortex breakdown. Unstationary surface pressure data needed for this comparison will be available from upcoming VFE-2 wind tunnel campaigns.

The blunt leading edge cases have shown two main problems associated with DES. In case 05, at lower AOA, advanced RANS methods guarantee a better evaluation of the boundary layer characteristics, leading to an increased accuracy in primary separation prediction. This is clear when studying the apex region and comparing the near-wall turbulence model of DES (SA) with EARSM. In this respect DES might be an inappropriate choice, but the increased accuracy in resolving primary vortex development, such as unstationary vortex breakdown phenomena, make it a valuable tool. Unfortunately, for blunt leading edge delta wings, the increased accuracy of DES in respect of vortex core development is negatively influenced by the model's capability to predict vortex separation onset, location and thus strength.

At higher AOA where the fully attached flow region is confined to the apex of the delta wing, both DES and EARSM resolve with similar accuracy the fore flow-field. Here, the unstationary and more accurate physical modeling of DES can be better exploited. At downstream positions a further weakness of DES appears; a computa-

tional grid, which is fine enough for RANS to achieve reasonable results, is probably too coarse in the LES region and no apparent improvement over RANS can be found.

5 Acknowledgments

The authors would like to thank the Swedish National Infrastructure for Computing (SNIC) for granting computational resources at the Center for Parallel Computers, KTH (PDC). Furthermore, the first author appreciated the prompt help provided by Dr. Peter Eliasson and Dr. Shia-Hui Peng (FOI) when problems arose with the solver. The fruitful discussions within the AVT-113/VFE-2 group, especially with Prof. D. Hummel and Dr. J. M. Luckring, are deeply appreciated.

References

- [1] Chu J and Luckring J. M. Experimental surface pressure data obtained on 65° delta wing across Reynolds number and Mach number ranges. Technical report, NASA Langley Research Center, Hampton, Virginia, 1996.
- [2] Crippa S and Rizzi A. Numerical investigation of Reynolds number effects on a blunt leading-edge delta wing. *Proc 24th AIAA Applied Aerodynamics Conference*, San Francisco, California, June 2006. AIAA.
- [3] Eliasson P. Edge, a Navier-Stokes solver for unstructured grids. *Proc Finite Volumes for Complex Applications III*, pp 527–534, 2002.
- [4] Elsenaar A and Eriksson G, editors. *International Vortex Flow Experiment on Euler Code Validation*. FFA, Flygtekniska Försökstanstalten, October 1986.
- [5] Hellsten A. *New Two-Equation Turbulence Model for Aerodynamics Applications*. PhD thesis, Department of Mechanical Engineering, Helsinki University of Technology (Espoo, Finland), 2004.
- [6] Hummel D. The second international vortex flow experiment (VFE-2) - objectives and first results. *Proc 2nd International Symposium on Integrating CFD and Experiments in Aerodynamics*, pp 1–12, Cranfield University (Shrivenham), UK, 2005.
- [7] Hummel D and Redeker G. A new vortex flow experiment for computer code validation. *Proc RTO AVT Symposium on Vortex Flow and High Angle of Attack Aerodynamics*, Loen, Norway, May 2001 2003.
- [8] Konrath R, Klein C, Engler R. H, and Otter D. Analysis of PSP results obtained for the VFE-2 65° delta wing configuration at sub- and transonic speeds. *Proc 44th AIAA Aerospace Sciences Meeting and Exhibit*, 2006.
- [9] Lamar J. E, Cronin C. K, and Scott L. E. A review of steps taken to create an international virtual laboratory at NASA Langley for aerodynamic prediction and comparison. *Progress in Aerospace Sciences*, Vol. 40, pp 163–172. Elsevier Ltd., UK, 2004.
- [10] Le Moigne Y. Adaptive mesh refinement and simulations of unsteady delta-wing aerodynamics. *Proc European Congress on Computational Methods in Applied Sciences and Engineering*. ECCOMAS, 2004.
- [11] Luckring J. M. Reynolds number and leading-edge bluntness effects on a 65° delta wing. *Proc 40th AIAA Aerospace Sciences Meeting and Exhibit*, 2002.
- [12] Spalart P, Jou W. H, Strelets M, and Allmaras S. R. Comments on the feasibility of LES for wings and on a hybrid RANS/LES approach. *Proc 1st AFSOR International Conference on DNS/LES*. Greyden Press, 1998.
- [13] Spalart P. R. Young-person’s guide to detached-eddy simulation grids. Technical report, NASA, 2001.
- [14] Spalart P. R and Allmaras S. R. A one-equation turbulence model for aerodynamic flows. *La Recherche Aéronautique*. ONERA, 1994.
- [15] Tysell L. An advancing front grid generation system for 3d unstructured grids. *Proc ICAS-94-2.5.1*, pp 1552–1564, 1994.
- [16] Tysell L, Berglund T, and Eneroth P. Adaptive grid generation for 3d unstructured grids. *Proc 6th International Conference on Numerical Grid Generation in Computational Field Simulation*, pp 391–400, 1998.
- [17] Wallin S and Johansson A. V. An explicit and algebraic Reynolds stress model for incompressible and compressible turbulent flows. *Journal of Fluid Mechanics*, Vol. 403, pp 89–132, 2000.